Characterisation of a horizontal axis wind turbine's tip and root vortices

Michael Sherry · John Sheridan · David Lo Jacono

Abstract The vortical near wake of a model horizontal axis wind turbine has been investigated experimentally in a water channel. The objective of this work is to study vortex interaction and stability of the helical vortex filaments within a horizontal axis wind turbine wake. The experimental model is a geometrically scaled version of the Tjæreborg wind turbine, which existed in western Denmark in the late 1980s. Here, the turbine was tested in both the upwind and downwind configurations. Qualitative flow visualisations using hydrogen bubble, particle streakline and planar laser-induced fluorescence techniques were combined with quantitative data measurements taken using planar particle image velocimetry. Vortices were identified using velocity gradient tensor invariants. Parameters that describe the helical vortex wake, such as the helicoidal pitch, and vortex circulation, were determined for three tip speed ratios. Particular attention is given here to the root vortex, which has been investigated minimally to date. Signatures of the coherent tip vortices are seen throughout the measurement domain; however, the signature of the root vortex is only evident much closer to the rotor plane, irrespective of the turbine configuration. It is postulated that the root vortex diffuses rapidly due to the effects of the turbine support geometries.

1 Introduction

Horizontal axis wind turbines (HAWT) are now an established means of producing renewable energy. Wind turbines have evolved greatly from the early machines implemented in Denmark in the 1980s to be the largest rotating machinery on Earth (Vermeer et al. 2003). There are two configurations of industrial scale horizontal axis wind turbines: upwind and downwind. In an upwind configuration, the supporting tower structure is downstream of the rotor assembly, whereas in a downwind configuration, the supporting tower is upstream of the rotor assembly. Advantages of downwind turbines include blade flexure away from the tower structure, reducing the risk of a blade-tower strike. They can also reduce wind misalignment in complex terrain with a vertical velocity component due to their negative tilt angle (Yoshida 2006). However, the inflow of a downwind turbine rotor necessarily contains the wake of the tower structure, the so-called 'tower shadow', causing cyclic loading on the blades, which can result in a source of unwanted aerodynamic noise and increased fatigue of turbine components.

As the lift-producing blades are upstream of the tower structure in an upwind turbine, it experiences a uniform inflow with no 'tower shadow'. The blades of an upwind turbine do, however, require greater rigidity to ensure a blade-tower strike does not occur. As the purpose of a wind turbine is to generate electricity through constant blade rotation and the overwhelming majority of turbines to date have been designed for uniform terrain conditions, most turbines currently installed are upstream turbines.

M. Sherry (✉) · J. Sheridan · D. L. Jacono
Fluids Laboratory for Aeronautical and Industrial Research (FLAIR), Department of Mechanical and Aerospace Engineering, Monash University, Melbourne, VIC 3800, Australia
e-mail: michael.sherry.au@gmail.com

D. L. Jacono
INPT, UPS, IMFT (Institut de Mécanique des Fluides de Toulouse), Université de Toulouse, Allée Camille Soula, 31400 Toulouse, France

D. L. Jacono
CNRS, IMFT, 31400 Toulouse, France

Wind turbines are designed to operate most efficiently in a specific wind speed regime and level of atmospheric turbulence. The conversion of the inlet kinetic energy into rotational motion of the blades creates a region of reduced velocity and increased turbulence intensity downstream of the turbine known as the wake. The energy conversion takes place through the generation of aerodynamic forces along the turbine blades.

Moreover, wind turbines are almost exclusively clustered in wind farms to yield the greatest energy from a given area and to share their distribution infrastructure. The interaction of a wind turbine's wake with another turbine in the cluster is an important wind farm design criterion. Wind turbine wake dynamics and interactions are thus important for turbines situated in wind farms. In particular, wind turbines located within a wind farm produce less energy than a stand-alone wind turbine due to the axial velocity deficit produced by the wake of other upstream turbines. The energy output of interior full-scale turbines in a wind farm ranges from 40 to 70 % of a stand-alone turbine (Barthelmie et al. 2011). The deficit depends on atmospheric stability, turbulence intensity and turbine density (Hansen et al. 2012). Increased sensing of inflow wind conditions coupled with individual blade pitch control of wake-affected turbines offers one possible mechanism to increase the collective efficiency of a wind farm.

A wind turbine wake can be broadly separated into two distinct regions: the near and far wake. The near wake is the region immediately downstream of a turbine where the effects of the rotating blades are evident. The near wake is strongly coupled to the aerodynamic efficiency of the wake-generating turbine; the far wake, on the other hand, commences when the effect of the wake-generating turbine is no longer visible and the wake is fully developed. Far wake effects are felt by downstream turbines in the cluster and are thus an important consideration in optimising wind farm efficiencies.

Estimates of the axial extent of the near wake range from $x/D \leq 1$ (Vermeer et al. 2003) to $2 < x/D < 5$ (Crespo et al. 1999). The point at which the near wake ends depends on atmospheric properties, such as stratification and turbulence intensity. The near wake is dominated by B counter-rotating helical vortex pairs, where B is the number of blades. A counter-rotating helical vortex pair consists of a tip and root vortex shed from each blade. Vortex structures are also shed from the turbine support geometries, including the tower and nacelle. In the absence of separated flow on the blade, vorticity is shed from a wind turbine blade where a spanwise gradient in bound circulation occurs. A tip vortex forms at the blade tip due to the three-dimensional (3D) flow generated by the pressure differential between the 'pressure' and 'suction' sides of the blade. The vorticity shed along the span of the blade

then rolls up into the coherent tip vortices in a similar fashion to the fixed-wing case due to the induced flow of the tip vortex. The tip and root vortex pathlines are helical in nature due to the rotating blades.

Horizontal axis wind turbines wakes have been investigated widely because of their importance in solving an important issue in the adoption of wind energy, and also because they represent an important and fundamental fluid dynamics problem. Wind turbine tip vortices have received most attention in the past because they are more easily visualised due to their position adjacent to the freestream flow, are usually stronger and have analogies to fixed and rotary aircraft. Tip vortices contain significant angular momentum which dictates the take-off and landing spacing of fixed-wing aircraft at airports. Rotary-wing aircraft are susceptible to blade-tip vortex interaction (BVI) in a powered descent, creating the unstable vortex ring state (VRS). The wake of a single wind turbine has been investigated using particle image velocimetry (PIV) by a number of researchers (Whale 1996; Grant and Parkin 2000; Dobrev et al. 2008; Schepers and Snel 2007). Whale (1996) compared his experimental data to a numerical code (Whale et al. 1996) and later full-scale field experimental data (Whale et al. 2000), achieving qualitative agreement. Grant and Parkin (2000) and Dobrev et al. (2008) both used a modified commercially available micro wind turbine for their research. Grant and Parkin (2000) investigated the effects of yaw misalignment, whereas Dobrev et al. (2008) captured planar data at a higher Reynolds number on several azimuthal planes. This latter study compared experimentally derived vortex evolution results to an analytical vortex model; it also qualitatively presented data on vortex meander (Dobrev et al. 2008) and postulated the increase in vortex meander with vortex age to an instability mechanism. Schepers and Snel (2007) provide an overview of the European MEXICO project where PIV was employed for the first time on a large-scale ($D = 4.5$ m) HAWT model. In the MEXICO program, tip vortex trajectories and properties were evaluated using stereo PIV data. Tip vortex strength corresponded well to the blade-bound circulation determined from blade pressure measurements (Schepers and Snel 2007). These studies provided information on tip vortex structure, but the root vortex was either not studied or could not be measured. This latter point is most probably due to the large diameter of the turbine hub and the fact that the lifting surface extended to the rotational axis in the Grant and Parkin (2000) and Dobrev et al. (2008) experimental models. The lifting surface in full-scale turbines typically ceases prior to the nacelle casing because of blade rigidity requirements.

Phase-averaged point measurements taken with a hot wire anemometer (HWA) (Medici and Alfredsson 2006; Ebert and Wood 2001) and a hot film anemometer (Haans

et al. 2008) have also been used to study wind turbine wakes. The Medici and Alfredsson (2006) study provided temporal information on the effect of turbulence on wake structure and the apparent presence of bluff body vortex shedding within wind turbine wakes. Ebert and Wood (2001) and Haans et al. (2008) investigated the 3D flow field in the very near wake ($x/D \leq 0.4$) and ($x/D \leq 0.3$), respectively, to avoid issues with vortex meander. Haans et al. (2008) applied an 'inverse wake method' to their experimental data to determine the blade loading and strength of the vortex system shed into the wake. The work highlighted the difficulty of measuring a coherent root vortex, with none being evident in the data despite the lifting surface terminating prior to the rotational axis (Haans et al. 2008). Ebert and Wood, on the other hand, measured coherent tip and root vortices in a series of papers (Ebert and Wood 1997, 1999, 2001). They captured the root/hub vortex and found that it was diffused rapidly by the nacelle boundary layer (Ebert and Wood 2001). Like the Grant and Parkin (2000) and Dobrev et al. (2008) studies, the lifting surface of the experimental model in the Ebert and Wood (2001) study extended all the way to the nacelle, which hampered root vortex formation. Micallef et al. (2011) used an inviscid panel code to show root vortices formed on their experimental model in which the lifting surface terminated in the root region. The root vortices persisted over their measurement domain ($x/R \leq 0.6$) adjacent to the nacelle section but no vortex characteristics were presented. The most recent review of the experimental work conducted in the area can be found in Vermeer et al. (2003).

Widnall (1972) investigated the stability of a single inviscid helical vortex filament subjected to sinusoidal perturbations. The study concluded that three instability modes affect helical vortex filaments. The modes depend on the perturbation wave number, γ, and specific filament properties, such as the vortex core radius to filament radius, r_{vc}/R, and the filament (helicoidal) pitch, h. The three modes are the high wave number (short wavelength) instability, low wave number (long wavelength) instability and a mutual inductance instability that occurs when the helicoidal pitch falls below a critical value (Widnall 1972). Widnall's (1972) analysis was purely theoretical with little resemblance to an operating rotor which generates multiple helical vortices. Gupta and Loewy (1974) independently applied a similar linear stability analysis to Widnall (1972) to a system of multiple helical vortices representing rotor wakes. They found the highest perturbation growth rates occurred when the deformation modes reduced the axial separation between adjacent helices. Ivanell et al. (2010) reached the same conclusion from LES computations. Okulov and Sørensen (2007), on the other hand, investigated the stability of a vortex system representative of a wind turbine or propeller far wake, where the helical tip vortices are embedded in a prescribed vortex flow field. The circulation of this flow field, Γ_{R+H}, represents that created by the hub and root vortices. The vortex system was found to be unconditionally unstable when the net circulation was zero, that is, $\Gamma_{R+H} = N\Gamma_T$, where Γ_T is the circulation of each tip vortex (Okulov and Sørensen 2007). Felli et al. (2011) recently investigated the stability of the helical vortex filaments created by a marine propeller with high-speed visualisations and documented both the short wave and mutual inductance instability modes (Felli et al. 2011). They concluded that the mutual inductance mode is the dominant mode leading to wake instability. Interestingly, results suggest that the perturbation arising from the tip vortex instability acts as the trigger for the root vortex instability (Felli et al. 2011).

Walther et al. (2007) performed numerical simulations of several points on the helical vortex filament stability map of Widnall (1972) at a finite Reynolds number using a massively parallelised vortex particle method code. They concluded that helical vortex filaments will inevitably break down under the effects of viscosity, with the process hastened by factors such as the helicoidal pitch and the radial separation distance between tip and root vortices (Walther et al. 2007).

From the literature involving the vortical structures (tip and root vortices) in a wind turbine wake to date, the degeneration of these structures in the near wake can thus be ascribed to the effect of freestream turbulence intensity, instability mechanisms which affect helical vortex filaments, cross-annihilation by vortices of opposite sign and viscous diffusion. The complete set of mechanisms and relative importance of each mechanism which leads to the degeneration of these coherent vortical structures are still relatively unknown. From both a fundamental fluid dynamics and practical perspective, it is important to understand how these helical vortical structures evolve in time and space.

The experiments described here were undertaken to gain insight into tip and root vortex structure and their interaction within a HAWT wake. This paper presents the first results of an experimental campaign underway at Monash University on wind turbine wake structure and stability. In addition to the characterisation of the tip vortices, particular focus was given to the root vortex evolution, as this has not been well documented in previous experimental studies of HAWTs. Mechanisms for the degeneration of the coherent root vortex are suggested based on the evidence gathered from the current experimental campaign and considerations of the effect the nacelle support geometries have on the flow structures in the wake. The authors acknowledge these mechanisms or hypotheses seemingly require further experimental evidence. The data required are being sought

in the continuing experimental campaign. The study additionally provides a sound database for validation of numerical models, particularly at low Reynolds numbers where there is presently a lack of data.

The experimental set-up is presented in Sect. 2, including the experimental technique and wind turbine model geometry used in the current tests. Preliminary flow visualisations depicting wake structure are also presented in Sect. 2. Section 3 presents the data post-processing methodologies used to elucidate the position and characteristics of the tip and root vortices. Following on in Sect. 4, wake structure results using the quantitative PIV technique are presented with individual vortex properties presented in Sect. 5.3. The degeneration of the root vortex structures is discussed in Sect. 5.5 prior to the main findings of the study and their consequences being summarised in Sect. 6.

2 Experimental set-up

The experiments were conducted in the fluids laboratory for aeronautical and industrial research (FLAIR) free-surface water channel. This facility has test section dimensions of $4,000 \times 600 \times 800$ mm and a freestream speed that can be varied between 60 and 460 mm/s. A scale model of the Tjæreborg wind turbine, which operated in western Denmark between 1988 and 1998, was constructed for the experiments. The Tjæreborg wind turbine was chosen as the model in the current study as it was documented for scientific research (Øye 1990, 1991) and has recently seen interest from numerical researchers (Ivanell et al. 2009). The original 3-blade upwind HAWT had a rotor diameter of 61 m and blades with both linear taper and twist (1°/3 m) (Øye 1990).

The airfoil used in the Tjæreborg turbine was from the NACA44XX family, with the model turbine limited to NACA4412 for ease of construction. Wind turbines are designed through an optimisation process using the blade element momentum (BEM) method (Glauert 1937). In the BEM method, the turbine blade is discretised into annular segments and the aerodynamic forces generated by the airfoil profile are calculated in each segment. To optimise the power coefficient of a wind turbine, each blade segment is configured to operate at or close to a design C_L/C_D ratio in the attached (linear) airfoil regime.

A wind turbine is optimised to operate at a single tip speed ratio, which is the ratio between the blades' tip speed and the freestream velocity, as defined in Eq. 1:

$$\lambda = \frac{\Omega R}{U_\infty}, \tag{1}$$

where Ω is the rotational speed of the turbine blades, R is the rotor radius and U_∞ is the freestream velocity. The

design tip speed ratio for the full-scale Tjæreborg turbine was $\lambda_{d,fs} = 7.07$ (Øye 1990).

The model turbine has a diameter of 230 mm with the swept area of the model producing a blockage ratio in the water channel of 8.6 %. The model is powered by an 18 V DC motor assembly, which is situated above the water channel surface and is connected to the main shaft of the model turbine by a toothed timing belt, which passes through the turbine support. The experimental set-up is shown in Fig. 3. The model turbine blades rotate in a counterclockwise direction when viewed from upstream. The turbine is synchronised with the data acquisition system through an optical encoder. The optical encoder allows measurements to be captured with a minimum angular displacement of 1°. Phase-locked averaged measurements (1 image acquisition per rotation) are presented here. Three tip speed ratios, $\lambda = 4, 7, 10 \pm 0.14$, were investigated, providing insight into both a lightly loaded rotor and heavily loaded rotor around the full-scale design condition, here rounded to $\lambda_d = 7$.

The tip speed ratio range using a freestream velocity, $U_\infty = 0.092$ ms^{-1}, gave a corresponding experimental Reynolds number range of $1,385 < Re_c < 3,369$. The Reynolds number ($Re = U_\infty D/v$) definition for the current model is given in Eq. 2,

$$
\begin{aligned}
Re_c(R) &= \frac{c_{tip} U_{rel}(R)}{v} \\
&= \frac{c_{tip}\sqrt{(U_\infty(1-a(R)))^2 + (\lambda U_\infty(1+a_t(R)))^2}}{v},
\end{aligned}
\tag{2}
$$

where c_{tip} is the blade tip chord, $a(R)$ and $a_t(R)$ are the axial and tangential interference factors at the tip and v is the kinematic viscosity of water. The relative velocity is assumed to consist of only the freestream and blade rotation components. The interference factors are introduced in Sect. 5. The Reynolds number of wind turbines in atmospheric conditions are several orders of magnitude larger than those in the experiments. The primary differences the Reynolds number dissimilarity will cause are a reduction in both the C_L/C_D ratio and $C_{L,max}$, stall of the blades at an earlier angle of attack, possible formation of a laminar separation bubble and enhanced diffusion of vortical structures. However, as turbulence levels in the atmospheric boundary layer are much greater than those simulated in the experimental conditions, the difference in vortex diffusion rates may be reduced because of the higher levels of turbulent diffusion of the coherent structures. The Reynolds number discrepancies will be discussed further in Sect. 4 below.
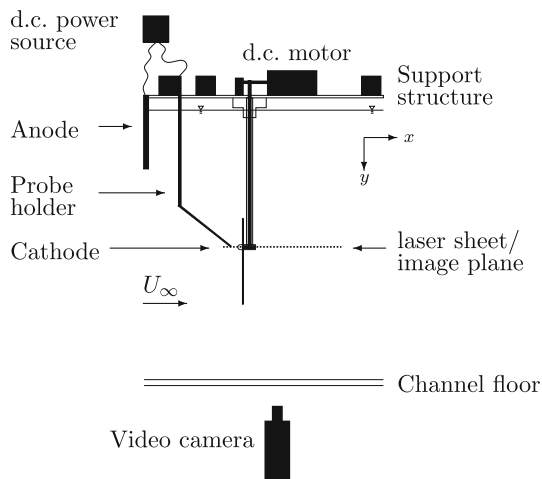
Both an upwind turbine configuration and downwind turbine configuration were tested with this experimental

arrangement. The model was studied in a downwind turbine configuration to investigate the effect on the root vortices of the vortex structures shed from the nacelle structures.
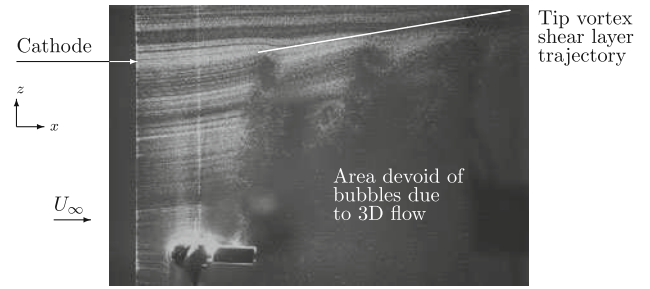
2.1 Preliminary flow visualisations

Qualitative data were initially captured with the hydrogen bubble (H2) and particle streaking flow visualisation techniques. A schematic of the H2 technique and the typical system is shown in Fig. 1.

A laser sheet passing through the rotational axis was used to illuminate a 2D (x-z) plane containing the tip and root vortices. The H2 probe was fixed in space, not the coordinate system of the rotating blades. The H2 technique seeded a 2D plane that was illuminated by the laser sheet. The visualisations were captured at a Reynolds number range of $0.75 \times 10^3 < Re_c < 1.967 \times 10^3$. These Reynolds numbers ensured bubbles reached a large enough size and also minimised any flow induced vibrations of the H2 probe. The visualisations were captured as both movies and phase-locked images that show the formation and interaction (where present) of the tip vortices as they advect downstream. A composite (average of several images) phase-locked image at $\lambda = 4$ is shown in Fig. 2. Here the flow is from left to right; the cathode is visible upstream of the blade. The tip vortices can be observed in Fig. 2 adjacent to the freestream flow by the areas devoid of tracer bubbles. A slight flow expansion is visualised by the deflection of the bubble traces in the positive z direction (i.e. radially outward). Because of the energy extraction

Fig. 2 Phase-locked averaged hydrogen bubble flow visualisation of an upwind turbine operating at $\lambda = 4$ and $Re_c = 1,600$, when viewed from the camera position shown in Fig. 1. Flow is from *left* to *right* with bubble generation by the cathode at the *left* of the image. Tip vortices visible as areas devoid of particles at wake boundary. A slight flow expansion is visible by the outward radial movement of the tip vortices. *Blade wakes*, *nose cone* and *nacelle* are also visible
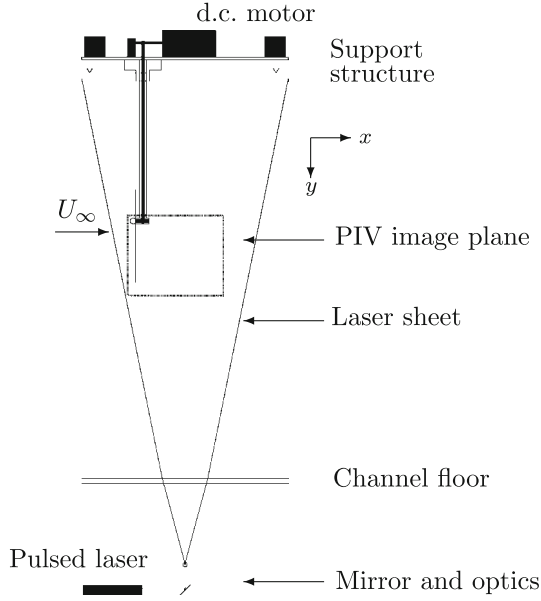
and blockage at the rotor plane, continuity requires that the flow expands in the wake. The region close to the wake centreline axis and behind the nacelle geometry is devoid of tracer bubbles due to the 3D flow caused by the nacelle. Three-dimensionality in the flow behind the nacelle removes the tracer bubbles from this plane and hence they no longer reflect the laser light, creating the dark region seen in the images.

2.2 Quantitative study

Quantitative wake field information was obtained from two-component PIV. The PIV measurement plane was aligned with the centreline axis of the wake, that is, the x-y plane as shown in Fig. 3. Due to the axial advection of the tip vortices and the corresponding skew angle of the wake, a measurement plane orthogonal to multiple tip vortex axes at any one instant is not possible. The skew angle at which the vortex axis intersects the measurement plane is deduced with a priori knowledge of the helicoidal pitch. This angle reduces with an increase in tip speed ratio.

The axial and radial velocity components in the wake were captured, allowing characterisation of the rotational motion in the image plane. From the sectional velocity data, vortical wake properties such as vortex core radius and the circulation for both the tip and root vortices were deduced. Measurements were phase averaged with a blade aligned with the tower structure and thus within the measurement plane. To avoid the vortical structures in the tower wake contaminating the phase-averaged data, only the top half of the wake ($y/R \geq 0$) was measured as shown in Fig. 3.

A pair of Nd:YAG lasers (Continuum Minilite PIV, USA) of wavelength 532 nm were used to produce pulsed laser sheets of 2 mm thickness. The lasers were situated under the water channel on a moveable trolley and their

Fig. 1 Side view of the experimental set-up of the hydrogen bubble (H2) rig used in flow visualisations. A single blade is aligned with the tower section in the phase-locked visualisations. Freestream flow, U_∞ is from *left* to *right* aligned with the positive x-axis. The x-, y- and z-axis follow a right-handed coordinate system. Channel depth reduced in figure. Images were captured in the x-z plane

Fig. 3 Experimental set-up of the wind turbine in an upwind configuration in the FLAIR water channel. Turbine is placed within channel in an inverted position. The freestream flow, U_∞, is from *left* to *right* aligned with positive *x*-axis, with the *y* and *z* axes following a right-handed coordinate system. The PIV image plane encompasses the region primarily behind the turbine blades in the near wake as indicated by the *rectangle*

beams directed into the channel by a mirror and lens set. The flow was seeded with polyamide particles of mean diameter 50 μm and specific gravity of 1.06 g/cm³.

A CCD camera (pco.4000, Germany) of resolution $4,008 \times 2,672$ pixels with a 105 mm AF micro lens (Nikkor, Japan) acquired the images for the phase-averaged measurements. The aperture of the lens was set to f5.6. A maximum magnification factor of 17 pixels/mm was employed giving a field of view (FOV) of $2.05R \times 1.37R$ in the axial and radial directions, respectively. A multi-step interrogation window with an initial size of 64×64 pixels to a final size of 32×32 pixels with 50 % overlap was used. This produced instantaneous velocity maps of 249 by 166 vectors. The vector resolution of the velocity maps was thus $8.2 \times 10^{-3}R$. A total of 300 image pairs were captured for each tip speed ratio and turbine configuration. Files of the wind turbine geometry coordinates for each flow configuration were used to avoid erroneous vectors arising from measurements made within the turbine's geometry contaminating the results. Validated in-house multi-pass cross-correlation PIV software was used to produce the velocity and vorticity fields (Fouras et al. 2008). Uncertainty in the PIV data can arise from random and bias components. The effect of the random components reduces with image number, here $N = 300$. For the random component of uncertainty, a sub-pixel peak fitting algorithm is incorporated in the PIV code resulting in 0.1 pixel

accuracy, corresponding to a uncertainty of $0.0427U_\infty$ (Raffel et al. 1998). The random error due to turbulence in the flow field can also be evaluated. The freestream turbulence intensity was $I_u \sim 1$ %. The fractional error estimation, ϵ, of the mean velocity is given by Eq. 3 (Grant and Owens 1990). Here ϵ is 0.135 % of U_∞, with a 98 % ($z_c = 2.326$) confidence level.

$$\epsilon = \frac{z_c I_u}{\sqrt{N}} \tag{3}$$

The calculated vorticity also has an uncertainty that arises from random and bias errors. Here, the vorticity was calculated using an algorithm that fits it with a 2D polynomial to minimise random and bias errors (Fouras and Soria 1998). Propagation of the random error from the velocity realisations (Fouras and Soria 1998) results in a non-dimensional vorticity uncertainty of 2.74 % with a 98 % confidence interval.

The post-processing methodologies used to elucidate both the position and structure of the tip and root vortices are presented next in the data analysis section.

3 Data analysis

The two-dimensional (2D) sectional velocity data acquired from planar PIV reveal the characteristic velocity and vorticity signatures of both the tip and root vortices. However, as the near wake contains strong velocity gradients particularly in the root region, vortex identification and characterisation using just the out-of-plane vorticity component, ω_z, shown in Eq. 4, are not feasible as vorticity does not necessarily denote a vortex.

$$\omega_z = \left(\frac{\partial v}{\partial x} - \frac{\partial u}{\partial y} \right) \mathbf{k} \tag{4}$$

The vortex core positions were identified by Galilean invariant local analysis techniques applied to the velocity gradient tensor, $\nabla \boldsymbol{u}_{2D}$. Following the critical point analysis of Chong et al. (1990), a vortex is defined here as "a region where the rate of deformation tensor is dominated by the rotation tensor". Critical point analysis techniques have been used to determine fixed-wing tip vortices from sectional PIV data (Carmer et al. 2008) and coherent structures (CS) in turbulent boundary layers (Chakraborty et al. 2005). The parameter used here is the swirling strength criterion formulated by (Zhou et al. 1999). A brief introduction of the swirling strength parameter follows.

Planar PIV captures displacement fields in two axes (here the axial and radial) $\{x, y\}$ which gives $\nabla \boldsymbol{u}_{2D}$ as,

$$\nabla \boldsymbol{u}_{2D} = \begin{bmatrix} \frac{\partial u}{\partial x} & \frac{\partial u}{\partial y} \\ \frac{\partial v}{\partial x} & \frac{\partial v}{\partial y} \end{bmatrix}, \tag{5}$$

where u and v are the velocities in the axial and radial directions, respectively. Spatial derivatives were evaluated using a second-order central differencing scheme.

If the discriminant, $\Delta = P^2 - 4Q$, of the characteristic equation, $\Lambda^2 + P\Lambda + Q = 0$ of matrix 5 is less than zero, the characteristic equation will have a complex conjugate eigenvalue pair, $\Lambda_{\text{r}} \pm \mathbf{i}\Lambda_{\text{ci}}$, where $\bullet_{\text{ci}}$ refers to the imaginary component. The imaginary component of the complex eigenvalues of matrix (5) is typically denoted by λ_{ci}; however, to avoid confusion here with the tip speed ratio, Λ_{ci} is used. Zhou et al determined that vortices correspond to regions with $\Lambda_{\text{ci}} > 0$, as particle trajectories about the real eigenvector axis have a finite time period of revolution $2\pi/\Lambda_{\text{ci}}$ (Zhou et al. 1999). Regions of shear in a fluid field have infinite revolution time periods and correspond to $\Lambda_{\text{ci}} = 0$. The method is thus able to discern between regions of shear and vortical motions and Λ_{ci} is a measure of the 'swirling strength' of a vortex (Zhou et al. 1999). The imaginary part of the complex eigenvalue, Λ_{ci}, is typically squared to improve the signal-to-noise ratio (SNR).

The velocity tensor methods allow accurate determination of instantaneous vortex core locations, minimising the effects of user-defined inputs and assumptions (common assumptions include solid body rotation in the vortex core or a circular integration path in circulation-based methods). The background level of Λ_{ci}^2 is determined from the free-stream flow measurements to account for turbulent structures within the freestream flow and measurement noise. An absolute definition of the threshold value $\Lambda_{\text{ci}}^* = \overline{\Lambda_{\text{ci}}^2} + 2\sigma_{\Lambda_{\text{ci}}^2}$ is used as a base value to determine the presence of vortical structures.

The instantaneous vortex core location is defined as the centroid of area of the minimum threshold Λ_{ci}^* contour encapsulating the Λ_{ci}^2 maximum (Vollmers 2001). Once a vortex has been identified, the circulation Γ is calculated via a line integral $\int_c \boldsymbol{u} \cdot \mathbf{d}l$, whose path, c, is the threshold contour, Λ_{ci}^*.

The Galilean invariant vortex identification methods described above give no indication of the direction of rotation of the vortical structures they identify. The vorticity in the fluid regions where the swirling strength parameter identifies a vortex is thus checked to determine the rotation of the vortex.

The following section outlines the results obtained from the phase-averaged PIV data.

4 Results

Phase averaging provides a snapshot of the vortices within the wake at a given instant in the blade rotational cycle. The phase-locked averaged wake axial velocity field for the full-scale design tip speed ratio $\lambda_{\text{d}} = 7$ is shown in Fig. 4. The flow is from left to right with the blade rotating in a counterclockwise direction when viewed from upstream. The blade is thus travelling out of the page in the negative z-direction. The effect of the wind turbine on the free-stream velocity is clearly evident from the phase-averaged velocity gradients present in the wake. To highlight these wake velocity gradients, velocity profiles at three axial locations, $x/R = 0.5, 1.0, 1.5$, are also shown on the right of Fig. 4. The velocity deficit increases as one moves near the wake centreline. A recirculation region forms immediately downstream of the nacelle with the mean region of reverse flow depicted by the dashed line in Fig. 4. This recirculation region was seen in numerical simulations of a number of nacelle geometries (Ameur et al. 2011). Particle streak flow visualisations in the root region (see Fig. 16 and text discussing this region in Sect. 5.5) indicate this flow is highly 3D. This restricts how definitively one can analyse this region of the wake when using the current planar experimental technique; however, a qualitative

Fig. 4 Phase-locked average wake of the Tjæreborg wind turbine operating in an upwind configuration at its full-scale design tip speed ratio ($\lambda_d = 7$). *Left*: Contours of axial velocity, $\overline{u}/U_\infty$, *dashed line* encapsulates region of mean reverse flow, and velocity gradients due to tip and root vortices are visible at the tip radius and close to nacelle, respectively. *Right*: Wake velocity profiles, $x/R = 0.5$ (*solid line*), $x/R = 1.0$ (*broken line*), $x/R = 1.5$ (*dotted line*)
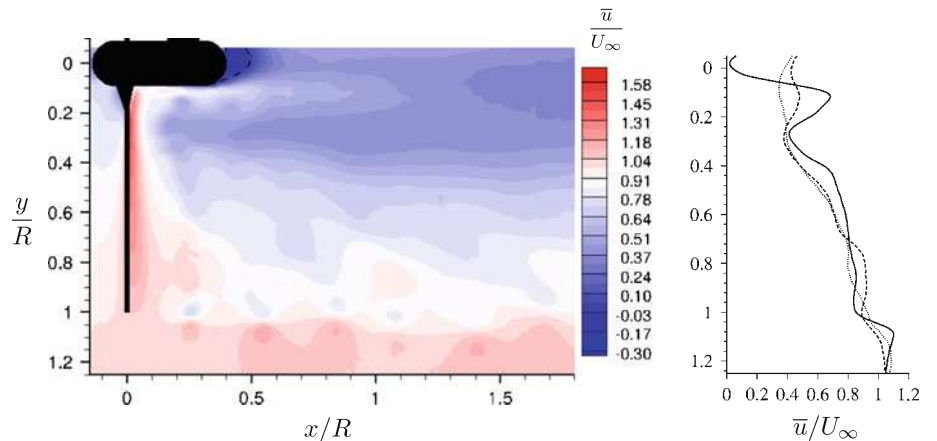
argument is made and supported. The nacelle geometry sheds vorticity which can in the very near wake form into a cylindrical vortex sheet centred on the wake centreline (Ebert and Wood 2001). In the present experimental set-up, the shedding process is complicated by the presence of the tower section and the pulsatile inflow created by the rotating blades. Beyond the nacelle recirculation zone, a central wake region of low velocity and high turbulence forms. Momentum recovery occurs downstream by viscous diffusion and turbulent mixing.

With increasing tip speed ratio, the model turbine acts like a solid disc which decreases the wake centreline velocity. Conversely, with a reduction in tip speed ratio, there is a corresponding increase in the wake centreline velocity. Momentum recovery thus occurs faster with reducing tip speed ratio. This is evident in Fig. 5 by the higher velocities and reduced spatial extent in the central wake region (for illustrative purposes, this is taken as $0.5\,U_\infty$). The wake velocity profile trends are, however, similar between the λ_d and $\lambda = 4$ cases.

As expected, $\lambda = 10$ (shown in Fig. 6) sees an increase in spatial extent of the central wake region and a decrease in velocity within this region with an increase in the tip speed ratio. This is clearly evident in the wake velocity profiles of Fig. 6. Despite the changes in central wake region structure with tip speed ratio, the maximum mean reverse flow in the nacelle recirculation zone remains largely independent of tip speed ratio. This maximum reached approximately 14 % of the freestream velocity in the tip speed ratios investigated. The recirculation zone extends furthest into the wake in the $\lambda = 4$ case, with reversed flow evident at $x/R = 0.5$ in Fig. 5.

Velocity gradients indicative of vortical structures can also be seen in Figs. 4, 5 and 6 at the unit radius and adjacent to the nacelle body, at $x/R \sim 0.15$. The tip and root vortices induce velocity components both in the direction of and opposing the mean streamwise flow. The tip vortices are located in the shear layer which forms between the freestream and retarded wake flow. The induced velocity components are most easily recognisable in the tip vortex shear layer when a wake velocity trace passes through a tip vortex. In this case, the axial velocity is both larger and smaller than the mean freestream velocity. These velocity gradients become weaker with axial distance at the experimental

Fig. 5 Phase-locked average wake of the Tjæreborg wind turbine operating in an upwind configuration below its full-scale design tip speed ratio ($\lambda = 4$). *Left*: Contours of axial velocity, $\overline{u}/U_\infty$, *dashed line* encapsulates region of reverse flow, and velocity gradients due to tip and root vortices visible at the tip radius and close to nacelle, respectively. *Right*: Wake velocity profiles, $x/R = 0.5$ (*solid line*), $x/R = 1.0$ (*broken line*), $x/R = 1.5$ (*dotted line*)
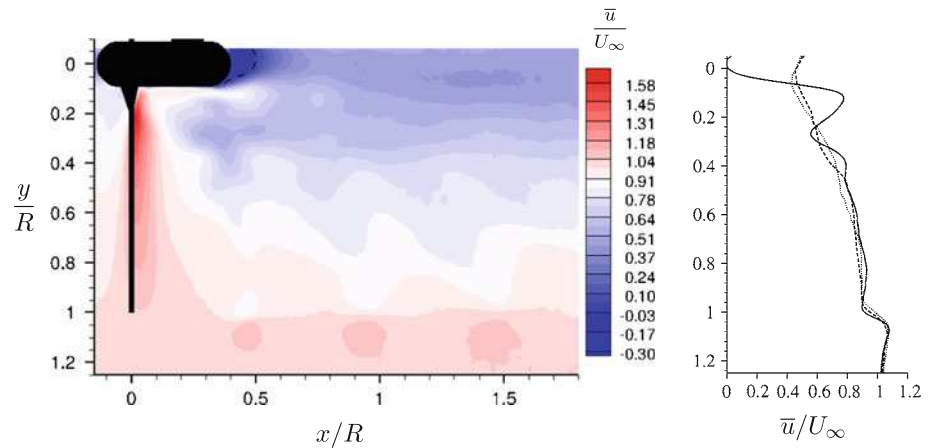
Fig. 6 Phase-locked average wake of the Tjæreborg wind turbine operating in an upwind configuration above its full-scale design tip speed ratio ($\lambda = 10$). *Left*: Contours of axial velocity, $\overline{u}/U_\infty$, *dashed line* encapsulates region of reverse flow, and velocity gradients due to tip and root vortices visible at the tip radius and close to nacelle, respectively. *Right*: Wake velocity profiles, $x/R = 0.5$ (*solid line*), $x/R = 1.0$ (*broken line*), $x/R = 1.5$ (*dotted line*)
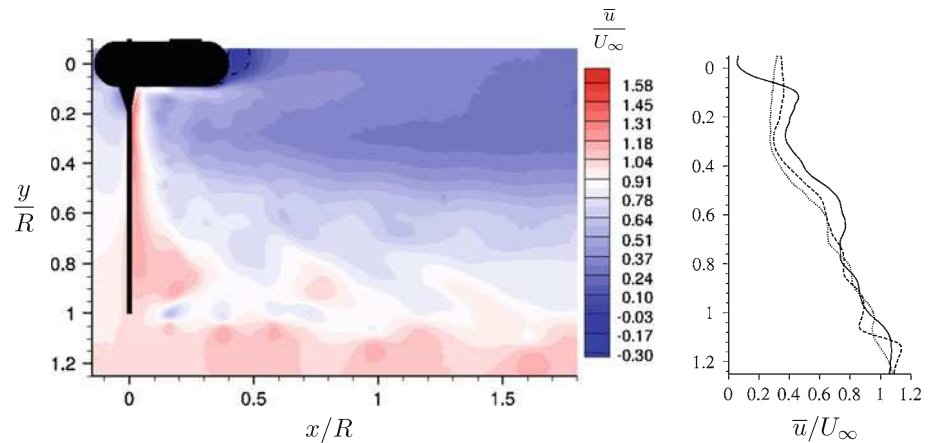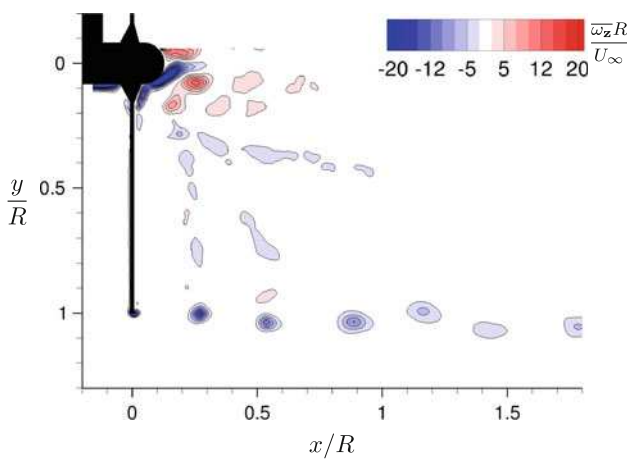
Reynolds number, primarily due to viscous diffusion, turbulent mixing and secondarily possibly due to instabilities arising in the vortices.

The velocity profiles change little between $x/R = 1$ and $x/R = 1.5$ for all tip speed ratios suggesting the wake velocity profile is close to a fully developed state. This alone would indicate a cessation of the near wake. However, as will be shown, tip vortices are present throughout the measurement domain indicating the transition to the far wake has not occurred.

The phase-locked average vortical wakes for λ_d are shown in Figs. 7 and 8 for a downwind and upwind turbine configuration, respectively. These figures show the out-of-plane vorticity, $\overline{\omega_z}$, within the near wake. In both Figs. 7 and 8, six tip vortices ($\omega_z < 0$) are visible in the shear layer around the unit radius. In addition, several root vortices ($\omega_z > 0$) are also present at small vortex ages (VA), close to the rotational axis ($y/R = 0.15$). The root vortex is designated as the coherent region of vorticity of opposite sign (positive) to the tip vortex closest to the rotational axis. The secondary peak of positive vorticity further radially outward ($y/R \sim 0.20$) of the root vortex is due to the blade wakes. 'Vortex age' is defined as the angular travel in degrees (°) of the blade which created the helical vortex filament.
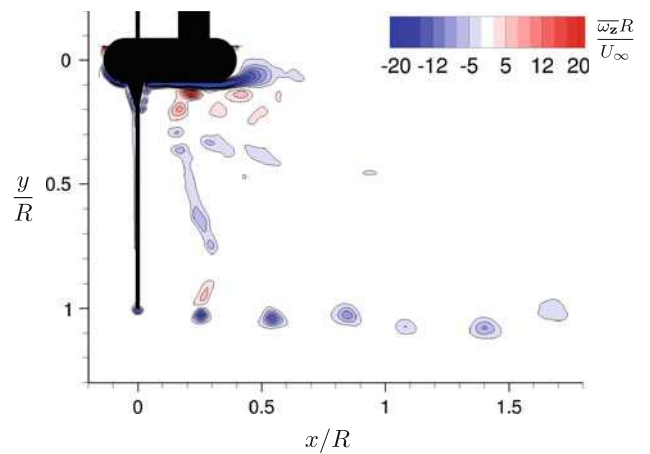
The Tjæreborg wind turbine was designed as an upwind turbine; however, at the model scale, the turbine could be easily tested in a downwind configuration. It is evident from Figs. 7 and 8 that the top half of the wake ($y/R \geq 0$) is affected little by the configuration of the model turbine. The most noticeable change between the two configurations occurs in the radial position of the root vortices, that is, the root vortex filament radius, R_r. The root vortex filament radius at a vortex age of 120° reduces by 70 %

between the downwind and upwind configurations. R_r reduces due to a net radial inward velocity which is impeded in an upstream configuration (Micallef et al. 2011). The bottom half ($y/R \leq 0$) of the wake will, however, display more pronounced differences due to the effects of tower shadow. The effect of tower shadow cannot be visualised in the current field of view employed. Testing in a downwind configuration allowed investigation of the effect that vorticity within the nacelle boundary layer has on the root vortices. This effect is discussed in further detail in Sect. 5.5.

Vorticity signatures of individual blade wakes can be seen in the region between the root and tip vortices in Figs. 8, 9 and 10. The blade wakes are the remnants of the
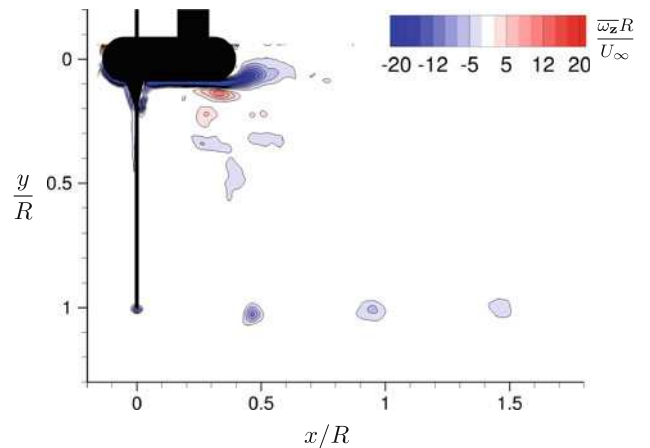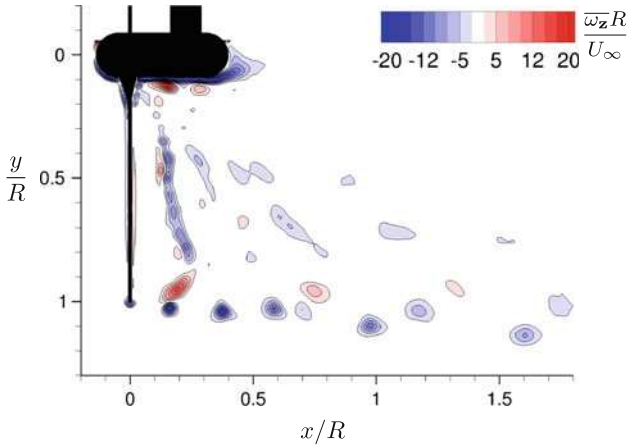

Fig. 8 Phase-locked average wake of the Tjæreborg wind turbine operating in an upwind configuration at the full-scale design tip speed ratio (λ_d) depicting the coherent vortical structures which dominate the near wake, contours of non-dimensional tangential vorticity, $\overline{\omega_z}R/U_\infty$

Fig. 7 Phase-locked average wake of the Tjæreborg wind turbine operating in an downwind configuration at the full-scale design tip speed ratio (λ_d) depicting the coherent vortical structures which dominate the near wake, contours of non-dimensional tangential vorticity, $\overline{\omega_z}R/U_\infty$

Fig. 9 Phase-locked average wake of the Tjæreborg wind turbine operating in an upwind configuration below its design tip speed ratio ($\lambda = 4$) depicting the coherent vortical structures which dominate the near wake, contours of non-dimensional tangential vorticity, $\overline{\omega_z}R/U_\infty$

Fig. 10 Phase-locked average wake of the Tjæreborg wind turbine operating in an upwind configuration above its design tip speed ratio ($\lambda = 10$) depicting the coherent vortical structures which dominate the near wake and the onset on instability, contours of non-dimensional tangential vorticity, $\overline{\omega_z}R/U_\infty$

vorticity sheet shed from each blade into the wake which has not yet rolled up into the coherent tip and root vortices. The induced velocities of the tip vortices cause the roll-up process such that with a vortex of low circulation, as in the present study, this process can be expected to take some time. The intensities of the blade wakes increase with tip speed ratio. The blade wakes also reveal the wake radial velocity gradient ($\partial U_x/\partial r$). The tip and root vortices become progressively less well aligned in the axial direction as they convect further downstream.

Post-vortex roll up, the tip vortices are adjacent to the higher velocity freestream fluid, in contrast to the root vortices, which are situated within the low-velocity central wake region. Although the mechanism for the difference in axial alignment is readily explainable, one cannot draw too many conclusions regarding trends of the growth of this differential due to the limited number of root vortex realisations. The speed of the root vortex diffusion is discussed further in Sect. 5.5

The wake structure of an upwind turbine operating below ($\lambda = 4$) and above ($\lambda = 10$) the design full-scale tip speed ratio (λ_d) is shown in Figs. 9 and 10, respectively. The axial distance a tip or root vortex travels in a single revolution reduces with increasing tip speed ratio as more vortices are shed into the wake. A single inviscid helical vortex filament is affected by the mutual inductance instability mode when the helicoidal pitch reduces below $0.3R$ (Widnall 1972). An ideal 3-bladed wind turbine wake consists of three counter-rotating helical vortex pairs. In reality, however, extra sources of vorticity are present in the form of the blade wakes and those shed from the turbine support structures. Thus, extrapolating the results of (Widnall 1972), the mutual inductance mode will act when the helicoidal pitch reduces below $0.9\ R$. Thus, the λ_d

(Fig. 8) and $\lambda = 10$ (Fig. 10) results are likely to be affected by this instability mechanism. As the helicoidal pitch reduces further below the critical pitch at which the instability mode first acts, the transition to instability occurs closer to the rotor plane (Felli et al. 2011). Felli et al. (2011) showed the mutual inductance instability mode was responsible for tip vortex entanglement. Qualitative evidence of the mutual inductance instability mode between adjacent tip vortices is evident at $x/R \sim 1$ in Fig. 8 and at $x/R \sim 0.7$ in Fig. 10. The non-uniform spacing in the axial and radial directions and the change in relative strength (vorticity) of the vortices at this location indicate the presence of the mutual inductance instability mode. The instability mode causes the instantaneous vortex positions to vary about the mean shown in the temporal averages. These deviations result in a spatial smoothing of vorticity.

A slight wake expansion is also seen in Figs. 8 and 10 immediately downstream of the rotor, as evidenced by the outward radial movement of the tip vortices. Wake expansion depends on the rotor loading and results from mass conservation, which is clear here from the axial velocity slow down. The axial position of the tip vortices follows a linear trend, as shown on the left in Fig. 11, whereas the radial core positions shown on the right in Fig. 11 vary more with vortex age. There is good agreement between the downwind and upwind axial positions of the tip vortices in the top half of the wake ($y/R \geq 0$), with the pitch of the upwind results slightly less than that of the downwind results. This difference probably arises due to variation in tip speed ratios. It is slightly larger than the bounds of uncertainty in the measurements at $\lambda = 4$. The difference generally decreases with increasing tip speed ratio.

5 Discussion

As the experimental model was not fitted with a force transducer, the thrust coefficient for the different flow cases was estimated using the blade element momentum method.

5.1 Blade element momentum method

The load on the rotor is calculated by coupling general 1D momentum theory and blade element theory, giving the so-called blade element momentum (BEM) theory. Modern-day BEM theory is attributed to Glauert (1937) and, despite the simplicity of the method, it is still the initial design tool of choice for wind turbine designers. In general momentum theory, the turbine is represented as an axisymmetric actuator disc. The theory produces the well-known Lancaster–Betz limit which states the maximum inlet kinetic

Fig. 11 Mean axial (*left*) and radial (*right*) position of the tip vortices with increasing vortex age. *Trend lines* have been applied to the axial positions only. *Dashed lines* and *hollow symbols*: downwind results; *solid lines* and *solid symbols*: upwind results
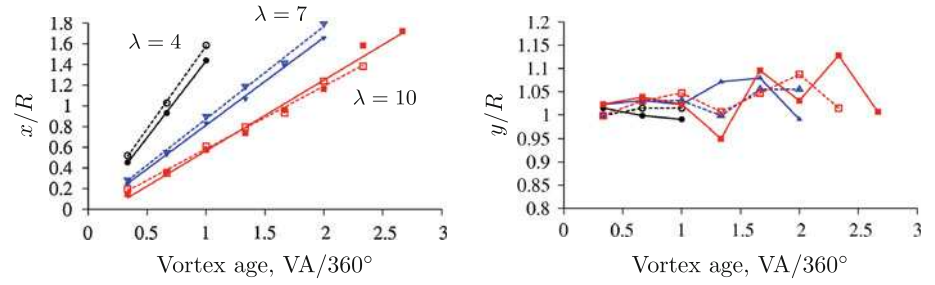
energy an axisymmetric disc can capture is 16/27, that is, $C_{P,\mathrm{max}} = 16/27$. The optimum axial interference factor, $\overline{a} = 1 - U_D/U_\infty$, where U_D is the velocity in the rotor plane, which produces this power coefficient is $\overline{a}_{\mathrm{opt}} = 1/3$. The tangential interference factor, on the other hand, $a_t = u_t/\omega r$, is the ratio between the induced azimuthal velocity in the rotor plane, u_t, and the rotor angular velocity. The interference factors a and a_t are thus a measure of the induced velocities in the axial and tangential directions. In blade element theory, the aerodynamic forces generated by the rotating blades are calculated at annular blade elements. The BEM method equates the aerodynamic forces generated at blade elements to the thrust and torque acting on the disc. The summation of all the blade element forces acting on an entire blade is thus the torque and thrust loading of the actuator disc. This total force is equated to the general momentum analysis to give an indication of the wake state the turbine operates within. One limiting factor of the BEM method is that it requires high-quality airfoil performance data as an input to calculate the blade element forces.

5.2 Blade model properties

The difference in Reynolds number between model and full scale introduces differences in the flow features seen on the airfoil. These differences are discussed here.

Airfoil performance is a strong function of chord-wise Reynolds number, Re_c. At low Reynolds numbers, airfoil performance is affected by a reduction in $C_{L,\mathrm{max}}$ and C_L/C_D and the possible formation of laminar separation bubbles. As an example, the maximum lift to drag ratio of the NACA4412 airfoil at a Reynolds number $Re_c \sim 6 \times 10^6$ is $C_L/C_D = 130$ (Øye 1990); however, as the Reynolds number decreases the drag experienced by the airfoil increases due to more pronounced viscous effects. The maximum C_L/C_D ratio of the NACA4412 airfoil reduces from ~ 36 at $Re_c = 8 \times 10^4$ to ~ 27 at $Re_c = 4 \times 10^4$ (Jacobs and Sherman 1937). This trend will continue with further reductions in Reynolds number. The maximum C_L/C_D ratio in the attached (linear) regime of an airfoil's performance curve (e.g. C_l and C_d vs. α) is used to predict the tip speed ratio for optimum rotor performance. For this

reason, the airfoil lift and drag characteristics at the model Reynolds number are needed to accurately predict the loads on the model turbine.

In addition to reduced aerodynamic performance at low Reynolds number, airfoils become susceptible to adverse flow features, such as laminar separation bubbles. The time-averaged flow features of a laminar separation bubble are shown in Fig. 12. The flow over airfoil profiles at low Reynolds numbers is susceptible to an adverse pressure gradient that leads to separation thus forming a separated shear layer. If turbulent transition takes place in the shear layer prior to the airfoil trailing edge, reattachment can occur creating a recirculation zone or 'bubble'. The recirculating flow in a laminar separation bubble causes an increase in pressure drag. Such laminar separation bubbles can 'burst', causing rapid separation from the leading edge and airfoil stall with a resulting increase in drag and reduction in lift.

Flow visualisations have shown separated shear layer reattachment, and hence laminar separation bubble formation, for a NACA0012 airfoil does not occur at $Re_c = 5.3 \times 10^3$ (Alam et al. 2010). An equivalent study of that by Alam et al. (2010) of cambered airfoils at low Reynolds numbers has not been undertaken to the authors'
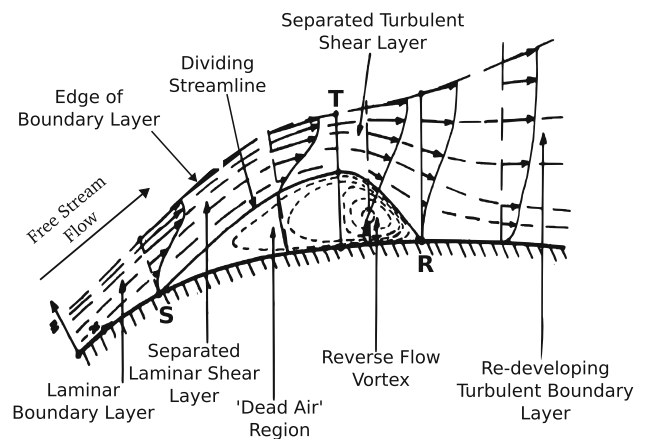
Fig. 12 Time-averaged flow features of a laminar separation bubble on the suction side of an airfoil. **S**: separation point, **R**: reattachment point, **T**: maximum vertical displacement where transition is most likely (Horton 1968)

knowledge. A cambered airfoil, such as the NACA4412 will be susceptible to boundary layer separation due to the increased surface curvature on the 'suction' side of the airfoil. Static flow visualisations were thus undertaken to determine whether laminar separation bubbles form on the NACA4412 in the Reynolds number range of the wind turbine experiments. The NACA4412 airfoil used had a chord of length 120 mm, allowing proper imaging of the boundary layer flow. The chord Reynolds number Re_c was 3,484. A continuous laser of wavelength 473 nm (blue) is formed into a sheet that illuminates the region of interest on the suction side of the blade from the leading to trailing edge. The chemical fluorescein was used to seed the flow. The laser causes the fluorescein to fluoresce allowing imaging of the flow physics.

The flow visualisations, shown in Fig. 13, indicate that laminar boundary layer separation occurs on the suction side of the airfoil. The separation point moves towards the leading edge with increasing angle of attack. Kelvin–Helmholtz (K–H) vortices intermittently form in the separated shear layer prior to the trailing edge at $\alpha = 15°$. The formation length of the K–H vortices reduces with increasing angle of attack. At $\alpha = 17.5°$, K–H vortices consistently form due to the separated shear layer prior to the trailing edge. Leading edge separation occurs at an angle of attack of $\alpha \sim 20°$. Further, turbulent transition does not occur in the separated shear layer prior to the trailing edge at $Re_c = 3,484$. The visualisations thus confirm for the first time that a laminar separation bubble does not form at this Re_c for the NACA4412 profile. Thus, the negative effects on airfoil performance caused by laminar separation bubbles (e.g. hysteresis and strong stall effects Selig et al. 1995) will be absent at the experimental Reynolds number. Consequently, the BEM method can be applied accurately to the experimental model, provided airfoil data at this Reynolds number are available.

Sunada and Kawachi (2002) investigated the lift and drag properties of a number of airfoil profiles including the Wortmann FX63-137 cambered airfoil, at a Reynolds number of $Re_c = 4 \times 10^3$. They found the maximum C_L/C_D ratio to be equal to 4.9 at an angle of attack of 7°. At very low reynolds numbers, mean thickness ratio and camber ratio are the most important airfoil characteristics for airfoil performance (Sunada and Kawachi 2002). The mean thickness ratio of the Wortmann FX63-137 (7 %) and the NACA4412 (7.2 %) is very similar such that the drag coefficient will be similar. Further, the Wortmann FX63-137 has a larger camber ratio (6 %) than the NACA4412 (4 %), so the maximum lift will be slightly larger in the former profile. However, the position of maximum camber is closer to the leading edge in the NACA4412, which produces a larger maximum C_L/C_D ratio (Sunada and Kawachi 2002). The NACA4412 and Wortmann FX63-137 airfoil profiles have similar performance at high Reynolds numbers, and their geometric similarity suggests their performance at low Reynolds numbers could also be similar. Based on this assumption, the cambered airfoil data of Sunada and Kawachi (2002) for $-20° \leq \alpha \leq 20°$ were used in conjunction with modified flat plate data of Blevins (1984) for $\alpha \leq -40°$ and $\alpha \geq 40°$. Airfoil performance becomes less dependent of airfoil shape in the fully stalled region, permitting the use of flat plate performance data. The magnitude of the Blevins (1984) flat plate data was reduced by 20 % to match the Sunada and Kawachi (2002) flat plate data at $Re_c = 4 \times 10^3$. Linear interpolation was performed between the two data sets. The modified airfoil data set was used with a standard BEM method (Hansen 2008), in conjunction with the tip and heavily loaded rotor correction formulas of Shen et al. (2005), to predict the model turbine loading.

Selected results of the BEM analysis on the model wind turbine are shown in Table 1. Results from a BEM analysis of the full-scale Tjæreborg wind turbine are also shown in the Table 1 in bold text, for comparison. $\langle \cdot \rangle$ indicates a spatial average taken in the spanwise direction. The subscript $\bullet_{PIV}$ indicates results from the PIV data. Table 1 indicates that the full-scale turbine operates close to its optimum efficiency at its design tip speed ratio of
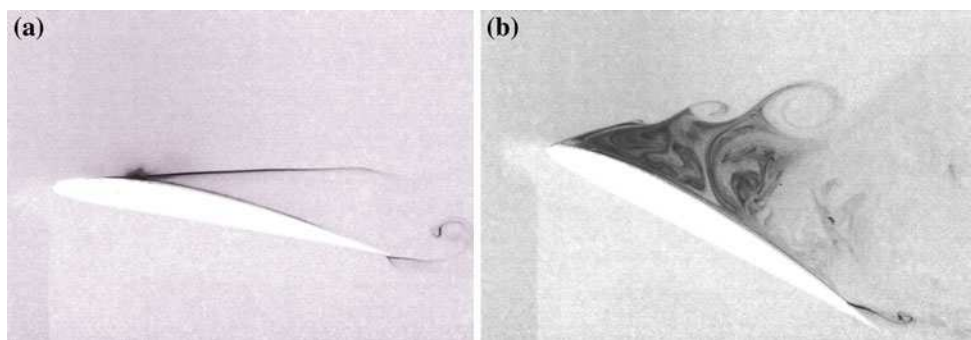
Fig. 13 Separated flow regimes over the NACA4412 airfoil (shown in *white*) at a Reynolds number of 3,484. *Dark areas* indicate fluorescein dye which images the separated shear layer. Flow from *left* to *right*. **a** $\alpha = 10°$, **b** $\alpha = 25°$

Table 1 BEM and PIV analysis of the experimental model in an upwind configuration and full-scale Tjæreborg wind turbine (bold text)

λ	$\langle \overline{a} \rangle$	$a_{\overline{\phi},\text{PIV}}$	$\langle \overline{a}_t \rangle$	$a_{t,\text{root}}$	$\Gamma_{B,\text{max}}/U_\infty R$	$\Gamma_{V,\text{PIV}}$	C_T
4	0.080	0.14	0.019	0.084	0.082	0.073 (0.064)	0.293
4	**0.131**	–	**0.030**	**0.103**	**0.143**	–	**0.452**
7	0.175	0.176	0.010	0.056	0.095	0.044 (0.073)	0.571
7.07	**0.343**	–	**0.023**	**0.010**	**0.137**	–	**0.890**
10	0.251	0.293	0.001	0.029	0.086	0.079 (0.089)	0.739
10	**0.473**	–	**0.012**	**0.051**	**0.133**	–	**1.071**

$\langle \overline{a} \rangle$: average axial interference factor, $a_{\overline{\phi},\text{PIV}}$: axial interference factor from PIV results as determined from Eq. 6, $\langle \overline{a}_t \rangle$: average tangential interference factor, $a_{t,\text{root}}$: root region ($x/R = 0.21$) tangential interference factor, $\Gamma_{B,\text{max}}/U_\infty R$: normalised maximum blade-bound circulation, $\Gamma_{V,\text{PIV}} = |\Gamma_T| + |\Gamma_R|$: sum of normalised circulation in the tip and root vortices at 120° (downwind results in brackets), C_T: thrust coefficient

$\lambda_{d,fs} = 7.07$ (i.e. $\langle \overline{a}(\lambda_{d,fs}) \rangle \approx \langle \overline{a}_{\text{opt}} \rangle = 0.33$). The average axial interference factor, $\langle \overline{a} \rangle$, for the experimental model increases with tip speed ratio whilst at all times remaining less than $\langle \overline{a}_{\text{opt}} \rangle$ and the full-scale values. In the absence of direct load measurements on the experimental model, the average value of the thrust coefficient along the blades, $C_T = \langle C_T(r) \rangle$, was used to give an indication of the loading of the model turbine. The thrust coefficient was evaluated using the axial interference factor and the BEM relations, $C_T(r) = 4\overline{a}(r)(1 - \overline{a}(r))$, where the rotor was treated as an actuator disc. As expected, the thrust coefficient increases with tip speed.

The blade-bound circulation distribution, $\Gamma_B(r)/U_\infty R$, is determined by applying the Kutta–Joukowski theorem to each annular segment. The circulation shed into the wake by a single blade, $\Gamma_V/U_\infty R$, is then determined by calculating the spanwise gradient, $\partial \Gamma_B(r)/\partial r$, of the blade-bound circulation. The trailing vortex system comprises vortices of strength corresponding to the incremental changes in the blade-bound circulation. Applying a zero loading ($\Gamma_B = 0$) condition at the tip and root, the strength of the tip and root vortices will each be the maximum blade-bound circulation value, $\Gamma_{B,\text{max}}/U_\infty R$. The maximum blade-bound circulation is highest at the design tip speed ratio for the experimental model but not at full scale. The average tangential interference factor reduces with increasing tip speed ratio, meaning less inlet kinetic energy is lost due to wake rotation. As expected, the full-scale turbine operates more efficiently than the model turbine due to the larger lift force produced by the blade segments.

Table 1 shows the suboptimum performance of the experimental model compared to the full-scale turbine.

The full-field PIV results can be compared against the BEM predictions. However, as data were only captured in the near wake, the velocity profile in the far wake is not available. Thus, the axial interference factor in the wake cannot be calculated directly from 1D momentum theory. Likewise, velocity measurements in the rotor plane are complicated due to the presence of the rotating blades. An alternate method to calculate the axial interference factor in the rotor plane is to assume the wake rotation, and hence, tangential interference factor is small. As the tip vortex advects downstream at the velocity at the blade trailing edge, the axial interference factor can be calculated from a velocity diagram of the blade crossing the plane of rotation, as shown in Fig. 14. The helix skew angle is equated to the angle the relative velocity, U_{rel}, makes with the plane of rotation, ϕ, as shown in Eq. 6.

$$\tan \phi = \frac{h}{2\pi r} = \frac{U_\infty(1 - a)}{\omega R(1 + a_t)} \tag{6}$$

Due to the pressure recovery occurring in the near wake, the pitch and vortex filament radius vary with vortex age. The upwind phase-averaged results at a vortex age of 120° were used in the analysis. Equation 6 can be simplified to produce a relation for the axial interference factor at the tip, $a(R) = 1 - \lambda \frac{h}{2\pi R}$. The pitch of the tip vortices determined from the PIV results was used to calculate the axial interference factor, $a_{\overline{\phi},\text{PIV}}$ at the tip. The phase-averaged axial interference factor from the PIV results, $a_{\overline{\phi},\text{PIV}}$, compares

Fig. 14 Velocity diagram at the rotor plane at a given spanwise location, r. The angle ϕ is the sum of α-local blade angle of attack and θ-local blade pitch angle
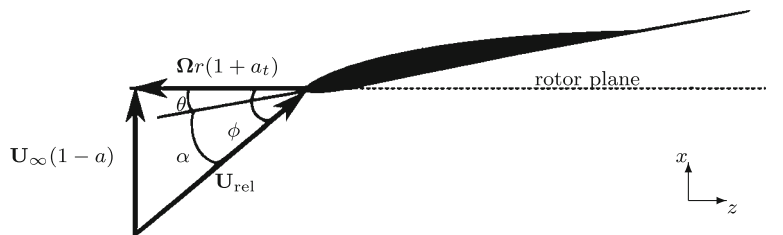
acceptably well with the BEM results. The largest discrepancy arises at the lowest tip speed ratio, where the assumption of negligible tangential induction is hard to justify. It is clear that the NACA4412 airfoil at this Reynolds number does not operate efficiently (low C_L/C_D ratio), which should be considered when devising low Reynolds number experiments to investigate wind turbine performance.

5.3 Vortex properties

Here the tip and root vortices shed into the wake by the three-bladed model wind turbine are characterised in an attempt to gain a deeper knowledge into their structure. Optimally in a uniformly loaded wing, for example, in the Prandtl wing or Joukowsky rotor, the summation of the spanwise blade-bound circulation gradient should be completely contained within the tip and root vortices. The maximum blade-bound circulation, $\Gamma_{B,max}/U_\infty R$, generated on the blades from a BEM analysis is indicated in Table 1. Using the data processing schemes outlined in Sect. 3, the circulations of the phase-locked average tip and root vortices were calculated. The sum of the tip and root vortex circulation ($\Gamma_{V,PIV} = |\Gamma_T| + |\Gamma_R|$) at a vortex age of 120° is shown in Table 1. The experimental results are approximately half that predicted by the BEM method and the LES computations of Ivanell et al. (2009) at $\lambda_{d,fs}$ and $Re_c = 1.6 \times 10^3$. The difference between the BEM predictions and the experimental results arises from the spanwise circulation gradient. The blade wakes visualised in Figs. 7, 8, 9 and 10 are evidence of the continual shedding of vorticity into the wake. With downstream distance, the blade wakes will be entrained by the tip and root vortices. There could also be an affect due to differences between the low Reynolds number performance of the current airfoil profile (NACA4412) and that used in the Sunada and Kawachi study (Wortmann FX63-137). In addition, the airfoil properties used in the BEM analysis are not corrected for 3D effects (Sørensen 2011), and it is known that airfoil performance increases with 3D effects especially in stalled regions. The BEM analysis indicated the percentage of the blade experiencing stall in the root region increases from 0.15 R to 0.47 R when λ reduces from 10 to 4. The stall angle was taken as 20° where separation occurs from the leading edge, as indicated in the flow visualisations. Ivanell et al's. (2009) results indicated the wake circulation derived from the velocity field agreed well with the blade-bound circulation when the circulation integral was performed on a plane perpendicular to the freestream, that is, a y-z plane. This analysis technique could not be used here due to the orientation of the measurement plane, that is, x-y as in Fig. 3.

5.4 Vortex meander

The core location of a single vortex advecting in a given flow domain (e.g. fixed-wing tip vortex) is known to experience fluctuations due to vortex meander (Devenport et al. 1996; Roy et al. 2011). The origins of vortex meander have been attributed to various flow field and geometry effects including wall boundary layer turbulence, freestream turbulence and surface irregularities (Beresh et al. 2010). Changes in the core structure have also been postulated to induce the meandering motion (Bandyopadhyay et al. 1991). Vortex meander of a multiple vortex system such as that in a wind turbine wake is more complex due to the helical nature of the vortex filaments and the interaction between vortices within the wake. As vortex meander was not the primary interest of this research, the data were analysed using the phase-locked averaging technique. However, the results still provided some insights into the meander of the tip and root vortices and some comment on the effect of vortex meander on vortex properties is presented here.

Accepting that the vortices meander, phase-locked averaging will spatially smooth vortex properties, such as maximum tangential velocity and core radius (r_{vc}) (Heyes et al. 2004). The vortex locations from each instantaneous PIV frame were extracted and compared to the temporal mean value of all frames. Uncertainty in the instantaneous vortex identification using Λ_{ci}^2 and the centroid of area method is estimated as ±4 pixels. Vortex meander is characterised by the standard deviation of the instantaneous vortex core position fluctuations on the two measurement axes, σ_x and σ_y. Devenport et al. (1996) assumed the meandering motions of fixed-wing tip vortices follow a gaussian distribution, allowing correction. A probability density function (pdf) of the instantaneous vortex core position fluctuations was thus created, and a gaussian profile fitted to the data (Devenport et al. 1996). The standard deviation σ_i was then extracted as a fitting parameter to characterise the extent of the meander at a given vortex age. The uncertainty on the meander magnitude is ±6 %.

Vortex meander results for the 300 PIV realisations are presented in Fig. 15. The trend lines in Fig. 15 indicate that tip vortex meander increases with vortex age. Physically, increased vortex meander is a possible indication of instabilities which arise along the helix. The large deviations from the trend particularly evident in the $\lambda = 10$ case can be attributed to the wake becoming unstable past $VA > 360°$. The trend lines indicate that a helical filament with a short helicoidal pitch is capable of resisting meander at early vortex ages. This can partially be attributed to the angle of attack in the tip region which reduces with

Fig. 15 Streamwise, σ_x, and radial, σ_y, tip vortex meander increase with vortex age, *dashed lines* and *hollow symbols*; downwind results, *solid lines* and *symbols*; upwind results, *black circle*: $\lambda = 4$, *blue triangle*: λ_d, red square: $\lambda = 10$
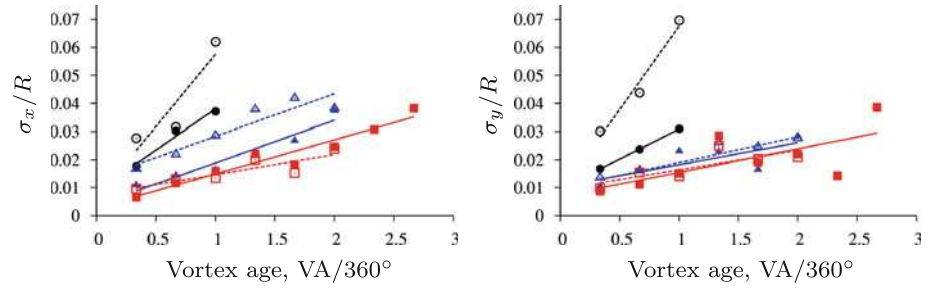
increasing tip speed ratio. With the current model, the angle of attack at the tip reduces from 13° to 5° when the tip speed ratio increases from 4 to 10. Attached flow in the tip region at higher tip speed ratios permits a more uniform (time invariant) pressure gradient between the pressure and suction airfoil surfaces to form. The PLIF visualisations (Fig. 13) indicated K–H vortices form in the separated shear layer. These K–H vortices affect the tip vortex roll-up process (vorticity entrainment) and will be a cause of meander. Thus, in the absence of flow separation on the airfoil, tip vortex formation will be steady at early vortex ages and meander arising during the roll-up process will be minimised.

It should be noted that at early vortex ages, a gaussian distribution is a good fit to the pdf of the tip vortex position deviations. The method of Devenport et al. (1996) was formulated for a single fixed-wing tip vortex. Such a vortex will only meander under its own influence or the aforementioned external influences. In a multi-vortex system such as a wind turbine wake, the induced velocity field of a single vortex acts as a perturbation to all other vortices in the field (via Biot–Savart law). Thus, it is not surprising that as the vortex age increases, the gaussian fit becomes less robust due to the likelihood of vortex interaction. A more robust vortex meandering characterisation procedure for vortices with helical symmetry forms part of the ongoing work.

As the vortex identification methodologies use gradient operators, results may be sensitive to experimental parameters such as the magnification factor. To check the dependence of the results on the magnification factor, a high-resolution data set of a single tip vortex at a tip speed ratio of 7 and vortex age of 120° was captured. The magnification factor was increased by a factor greater than 4 to 77.95 px/mm. The high-resolution data produced a phase-averaged maximum swirling strength of 27.89 compared to 12.37 obtained with the lower magnification factor. The vortex locations, however, were almost identical. Therefore, whilst there is some dependence on the experimental parameters, it is important to note that vortex position was unaffected by the magnification factor.

5.5 Root vortex behaviour

This section outlines the influences that lead to the rapid diffusion/destruction of the root vortex. The interaction of the rotating blades and the turbine support structures with the fluid makes the flow in the root region of a wind turbine highly complex (Zahle and Sørensen 2011). The approaching flow interacts with the rotating nose cone and a 3D boundary layer forms. In an upwind turbine configuration, the boundary layer is then stretched around the root section of the blades with an analogy to a fixed cylinder on a ground plate. A horseshoe vortex system progresses downstream with helical symmetry. Ebert and Wood (2001), however, showed this vortex structure is cancelled by the root vortex quickly due to the angular momentum imparted by the rotating blades. In addition, on most full-scale turbines (the Enercon E-126 is an exception), the blade lifting surface terminates prior to the rotational axis to ensure they remain rigid. Zahle and Sørensen (2011) showed that cylindrical blade sections generate a von Kármán vortex street.

Particle streak flow visualisations also highlighted a flow feature of the experimental model that may not feature on full-scale turbines. The visualisations were captured at a sample rate of 100 Hz with a high-speed camera (IDT Redlake X3) in conjunction with a green continuous wave laser of wavelength 532 nm. As found on a number of full-scale turbine models, the experimental model had a small gap between the rotor assembly and the nacelle. This is typically disregarded in numerical simulations (Masson and Smaïli 2006; Ameur et al. 2011; Zahle and Sørensen 2011). However, this gap produced a rotating cavity flow that was periodically expelled when a root vortex passed the gap. Figure 16 shows the advection of a root vortex downstream in a 120° segment of the wake. Images are chosen to highlight the root vortex structures and are not equi-spaced in the 120° segment. The flow is from left to right with the blade rotation in a counterclockwise direction when viewed from upstream. The labels 'rv1' and 'rv2' indicate the position of root vortices within the field of view. The streaklines of the root vortices do not form closed loops as the vortex axis is not aligned with the

Fig. 16 Particle streak flow visualisation sequence in the x-y plane (120° progression **a**–**d**) showing blade passage, rotating cavity flow (below *rc* marker and *white circles*), root vortex (above *rv1* and *rv2* markers) passage and recirculation region (marker *rr*) behind nacelle. *Bottom images*, expanded view of *white circle* regions. Flow from *left* to *right*, λ_d, $Re_c = 2$ 900, particle streak lengths show qualitative instantaneous velocities
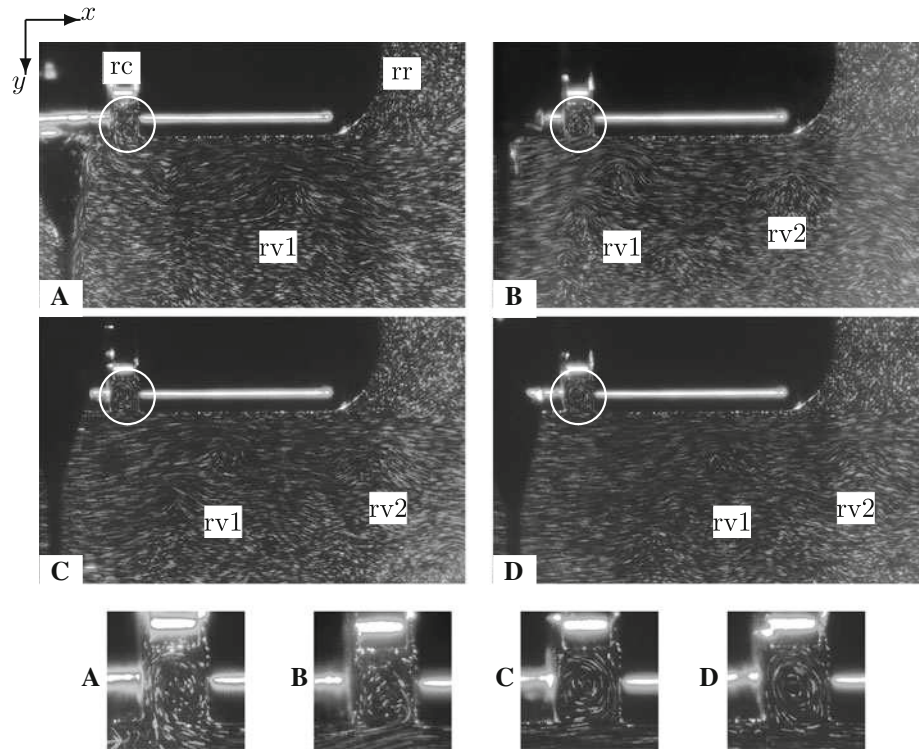
image plane due to the skew angle of the wake. Furthermore, the root vortex advects at a different velocity to the flow field due to the axial induction produced by the blades. The label 'rc' and white circles denote the rotating cavity flow which is expelled with a passage of a root vortex. Expanded views of the cavity region are shown in the views below the main images. The rotating cavity flow is most visible in images C and D when the phase of the blade is not aligned with the measurement plane. The cavity flow rotation is of opposite orientation to that of the root vortex, which will destabilise the root vortex. The label 'rr' indicates the recirculation region downstream of the nacelle as indicated by the dashed contour line in Figs. 4, 5 and 6.

Coherent root vortices can be seen in Figs. 7, 8, 9 and 10 at early vortex ages depending on tip speed ratio ($VA \leq 360°$), but the signal weakens soon after. The root vortex core to filament radius ratio, r_{vc}/R_r, is larger than the tip vortex value which causes an increase in the amplification rate of the mutual inductance instability mode leading to earlier breakdown (Widnall 1972). The numerical study by Ivanell et al. (2009) indicated that the small radius of curvature of the root vortex helix and the close proximity of adjacent helix turns are the primary reasons for instabilities arising in the root vortex signal. As in the current results, the root vortices became unstable prior to the tip vortices (Ivanell et al. 2009). Felli et al. (2011), however, showed using flow visualisations, that for a propeller wake, the root vortex transitions to instability due to

a perturbation caused by an unstable tip vortex (i.e. after the tip vortex). In addition to the previously mentioned causes of the early onset of instabilities arising in the root vortex, helical vortex filaments emanating from field turbines and scale experimental models will also be affected by the turbine support structures.

The rapid destabilisation of the root vortices in an upwind turbine wake is postulated to be primarily due to three phenomena. Firstly, the root vortices are in close proximity to the nacelle boundary layer; secondly, the root vortex must interact with the tower section; and lastly, the root vortices envelope the low-velocity fluid in the central wake region immediately downstream of the nacelle. Operating the model turbine in a downwind configuration allowed decoupling of the root vortex tower interaction phenomena, hence the root vortices shed in a downwind turbine configuration are subjected to the first and third phenomena only. As upwind turbines are the most prevalent installed turbines, the three effects will now be discussed further in terms of an upwind turbine configuration.

5.5.1 Nacelle boundary layer vorticity

The vorticity created within the nacelle boundary layer is shown immediately adjacent to the nacelle in Figs. 7, 8, 9 and 10. It is of the same order of magnitude and opposite in sign to the coherent root vortices, meaning there will be cross-annihilation of vorticity at the vortex core boundaries. Ebert and Wood (2001) showed through axial

vorticity contours in the very near wake that the root vortices of their experimental model merged into a single columnar 'hub' vortex centred on the rotational axis. The merging occurred in a shorter distance with increasing tip speed ratio. Zahle and Sørensen (2011), on the other hand, found the flow in the nacelle region to be highly complex and dependent on the flow speed and yaw angle. In their simulations of a full-scale turbine, axial vorticity contours at the end of the nacelle ($x/R = 0.36$) showed the nacelle boundary layer and three counter-rotating vortices per blade. The three vortices correspond to the root vortex and the von Kármán vortices from the cylindrical sections of the blade in the root region. The lifting surface terminated prior to the rotational axis in the Zahle and Sørensen (2011) study, which was not the case in the model of Ebert and Wood (2001). Zahle and Sørensen (2011) noted the three vortices interact causing high-velocity gradients in the root region. However, no information was presented on how they evolve. The presence of an equivalent 'hub' vortex to the Ebert and Wood (2001) study cannot be realised here due to the orientation of the planar experimental technique.

5.5.2 Root vortex tower interaction

Due to the small radius of curvature of the helix of the root vortex, the root vortices will be affected by their interaction with the tower section, here denoted as root vortex tower interaction (RVTI). The root vortex cannot pass the tower section unaltered. This interaction will create a perturbation in the root vortex possibly leading to an instability and early breakdown. However, with the small induced tangential velocity component in the root section as shown in Table 1 and the fixed measurement reference frame, the effects of RVTI are unlikely to be seen in the current data.

5.5.3 Central wake region

At axial locations greater than the length of the nacelle, the root vortices are subjected to the low-velocity fluid immediately downstream of the nacelle section. This region is visible in Fig. 16, indicated by 'rr'. Flow visualisations indicated this region is highly turbulent and 3D due to the pulsatile inflow created by the rotating blades. There is also momentum transfer occurring between the outer regions of the wake and the central wake region. The three-dimensionality and the turbulent nature of the fluid in this region promotes instabilities leading to breakdown of the coherent root vortex structures.

5.5.4 Root vortex destabilisation

It has been shown that the root vortex lies in close proximity to numerous factors which could cause its

destabilisation. In addition to the instability modes affecting helical vortex filaments (Widnall 1972), three additional mechanisms for their rapid destabilisation were proposed. Root vortex tower interaction (RVTI) will occur in the bottom half of the wake ($y/R \leq 0$) causing rapid vortex destabilisation. RVTI effects were not imaged in the current field of view due to the small tangential induction created by the blades. RVTI characterisation forms part of the ongoing works.

The rapid destruction of the root vortices seen in Figs. 7, 8, 9 and 10 can thus be attributed to the presence of vorticity of opposite sign within the nacelle boundary layer and the turbulent central wake region. The turbine was tested in a downwind configuration to displace the effect of cross-annihilation of root vortex vorticity by the nacelle boundary layer vorticity. However, the root vortices in the downwind (Fig. 7) and upwind (Fig. 8) configurations persist to a similar axial extent ($x/R \sim 0.6$) suggesting that cross-annihilation of vorticity is of secondary importance to the central wake region fluid. Panel code simulations by Micallef et al. (2011) showed the root vortex exists across their entire domain ($x/D \leq 0.6R$). The fluid within the central wake region had no effect on the root vortices because the length of the nacelle was greater than $x/D \leq 0.6R$ (Micallef et al. 2011).

The root vortices in a wind turbine wake are destabilised by a multitude of mechanisms including the three instability modes affecting helical vortex filaments (Widnall 1972) and the three additional mechanisms outlined in this section. Results from the present experimental model suggest that the central wake region is a dominant mechanism leading to root vortex destabilisation.

6 Conclusion

The wake structure of a model horizontal axis wind turbine based on the Tjæreborg field turbine has been investigated in a water channel facility using flow visualisation techniques and planar particle image velocimetry. Three tip speed ratios were investigated corresponding to a lightly loaded, design load and heavily loaded full-scale rotor condition. The wake structure varied with tip speed ratio as expected. The low-velocity central wake region behind the nacelle increased in size with increasing tip speed ratio. The helicoidal pitch reduced with increasing tip speed ratio causing the wake to become unstable closer to the rotor plane. The magnitude of the meandering motion of the tip vortices was characterised in the near wake. Results suggested vortex meander in this multiple vortex system increases with vortex age. The present results also indicate a reduction in helicoidal pitch serves to suppress meandering motions until the wake becomes unstable. This

phenomena were attributed to the absence of K–H vortices in the separated shear layer at higher tip speed ratios. Once the wake becomes unstable, the meander magnitude fluctuates more about the linear trends applied to the results. Vortex meander is thus proposed as an indication of instabilities forming along the helical filaments.

In addition to characterisation of the tip vortex structure, particular attention is given to the root vortex. The rapid destabilisation of the coherent root vortex can be attributed to a combination of the instability mechanisms affecting helical vortex filaments and three factors caused by the turbine support geometries. The latter are instabilities introduced along the filament by the root vortex tower interaction (RVTI); cross-annihilation of root vortex vorticity by the nacelle boundary layer vorticity; and finally, the low-velocity fluid directly behind the nacelle section is three-dimensional in nature leading to perturbations of the root vortex filaments. Through a process of testing the turbine in different configurations, the results indicate the central wake region has a pronounced affect on root vortex stability.

The blade airfoil properties at the experimental Reynolds number differed significantly to those of the full-scale turbine. It may be concluded these differences had a pronounced effect on the wake structure. It is thus advisable to consider airfoil performance when designing low Reynolds number rotary or fixed-wing experiments. The results highlight the coupled nature of the aerodynamics of the blade elements and near wake structure. Phase-averaged data were suitable to provide general wake structure information but the effect of vortex meander on vortex properties must be considered.

References

Alam MM, Zhou Y, Yang H, Guo H, Mi J (2010) The ultra-low Reynolds number airfoil wake. Exp Fluids 48:81–103

Ameur K, Masson C, Eecen P (2011) 2D and 3D numerical simulation of the wind-rotor/nacelle interaction in an atmospheric boundary layer. J Wind Eng Ind Aerodyn. doi:10.1016/j.jweia.2011.06.002

Bandyopadhyay P, Stead D, Ash R (1991) The organized nature of a turbulent trailing vortex. AIAA J 29(10):1627–1633

Barthelmie R, Frandsen S, Rathmann O, Hansen K, Politis E, Prospathopoulos J, Schepers J, Rados K, Cabezón D, Schlez W, Neubert A, Heath M (2011) Flow and wakes in large wind farms: final report for upwind wp8. Tech. Rep. Risø-R-1765(EN), Risø DTU, National Laboratory for Sustainable Energy

Beresh S, Henfling J, Spillers R (2010) Meanser of a fin trailing vortex and the origin of its turbulence. Exp Fluids 49(3):599–611

Blevins R (1984) Applied fluid dynamics handbook. Van Nostrand Reinhold company, New York

Carmer C, Konrath R, Schroder A, Monnier J-C (2008) Identification of vortex pairs in aircraft wakes from sectional velocity data. Exp Fluids 44:367–380

Chakraborty P, Balachandar S, Adrian R (2005) On the relationships between local vortex identification schemes. J Fluid Mech 535:189–214

Chong M, Perry A, Cantwell B (1990) A general classification of three-dimensional flow fields. Phys Fluids A 2(5):765–777

Crespo A, Hernández J, Frandsen S (1999) Survey of modelling methods for wind turbine wakes and wind farms. Wind Energy 2:1–24

Devenport W, Rife M, Liapis S, Follin G (1996) The structure and development of a wing tip vortex. J Fluid Mech 312:67–106

Dobrev I, Maalouf B, Troldborg N, Massouh F (2008) Investigation of the wind turbine vortex structure. 14th international symposium on applications of laser techniques to fluid mechanics, Lisbon, Portugal, 07–10 July 2008

Ebert P, Wood D (1997) The near wake of a model horizontal-axis wind turbine, part 1. Experimental arrangements and initial results. Renew Energy 12(3):225–243

Ebert P, Wood D (1999) The near wake of a model horizontal-axis wind turbine, part 2. General features of the three-dimensional flowfield. Renew Energy 18:513–534

Ebert P, Wood D (2001) The near wake of a model horizontal-axis wind turbine, part 3. Properties of the tip and hub vortices. Renew Energy 22:461–472

Felli M, Camussi R, Felice FD (2011) Mechanisms of evolution of the propeller wake in the transition and far fields. J Fluid Mech 682:5–53

Fouras A, Soria J (1998) Accuracy of out-of-plane vorticity measurements derived from in-plane velocity field data. Exp Fluids 25:409–430

Fouras A, Lo Jacono D, Hourigan K (2008) Target free stereo piv: a novel technique with inherent error estimation and improved accuracy. Exp Fluids 44:317–329

Glauert H (1937) The elements of airfoil and airscrew theory. Cambridge University Press, London

Grant I, Owens E (1990) Confidence interval estimates in PIV measurements of turbulent flows. Appl Opt 29(10):1400–1402

Grant I, Parkin P (2000) A DPIV study of the trailing vortex elements from the blades of a horizontal axis wind turbine in yaw. Exp Fluids 28:368–376

Gupta B, Loewy R (1974) Theoretical analysis of the aerodynamic stability of multiple, interdigitated helical vortices. AIAA J 12(10):1381–1387

Haans W, van Kuik G, van Bussel G (2008) The inverse vortex wake model: a measurement analysis tool. J Solar Eng 130:1–14

Hansen K, Barthelmie R, Jensen L, Sommer A (2012) The impact of turbulence intensity and atmospheric stability on power deficits due to wind turbine wakes at horns rev wind farm. Wind Energy 15:183–196

Hansen M (2008) Aerodynamics of wind turbines, 2nd edn. Earthscan, London

Heyes A, Hones R, Smith D (2004) Wandering of wing-tip vortices. In: Proceedings of 12th international symposium on the applications of laser techniques to fluid mechanics. Lisbon, Portugal

Horton H (1968) Laminar separation bubbles in two and three-dimensional incompressible flow. PhD, University of London

Ivanell S, Sørensen J, Mikkelsen R, Henningson D (2009) Analysis of numerically generated wake structures. Wind Energy 12:63–80

Ivanell S, Mikkelsen R, Sørensen J, Henningson D (2010) Stability analysis of the tip vortices of a wind turbine. Wind Energy 13(8):705–715

Jacobs E, Sherman A (1937) Airfoil section characteristics as affected by variations of the Reynolds number. Tech. Rep. Report No. 586, National advisory committee for aeronautics

Masson C, Smaïli A (2006) Numerical study of turbulent flow around a wind turbine nacelle. Wind Energy 9:281–298

Medici D, Alfredsson P (2006) Measurements on a wind turbine wake: 3D effects and bluff body vortex shedding. Wind Energy 9:219–236

Micallef D, Akay B, Saint T, Ferreira C, van Bussel G (2011) Experimental and numerical study of radial flow and its contribution to wake development of a HAWT. In: Proceedings of the European wind energy association

Okulov V, Sørensen J (2007) Stability of helical tip vortices in a rotor far wake. J Fluid Mech 576:1–25

Øye S (1990) Tjæreborg wind turbine (Esbjerg) geometric and operational data. Tech. Rep. AFM-NOTAT VK-184, Department of fluid mechanics, DTH

Øye S (1991) Tjæreborg wind turbine (Esbjerg), first dynamic inflow measurement. Tech. Rep. AFM-NOTAT VK-189, Department of fluid mechanics, DTH

Raffel M, Willert C, Kompenhans J (eds) (1998) Particle image velocimetry—a practical guide. Springer, Heidelberg, pp 51–58; 182–189

Roy C, Leweke T, Thompson M, Hourigan K (2011) Experiments on the elliptic instability in vortex pairs with axial core flow. J Fluid Mech 677:383–416

Schepers J, Snel H (2007) Model experiments in controlled conditions, final report. Tech. Rep. ECN-E–07-042, Energy research centre of the Netherlands

Selig M, Guglielmo J, Broeren A, Giguére P (1995) Summary of low-speed airfoil data, vol 1. SoarTech Publications, Virginia Beach, VA

Shen W, Mikkelsen R, Sørensen J (2005) Tip loss corrections for wind turbine computations. Wind Energy 8:457–475

Sørensen J (2011) Aerodynamics aspects of wind energy conversion. Annu Rev Fluid Mech 43:427–448

Sunada S, Kawachi K (2002) Comparison of wing characteristics at an ultralow Reynolds number. J Aircr 39(2):331–338

Vermeer L, Sørensen J, Crespo A (2003) Wind turbine wake aerodynamics. Prog Aerosp Sci 39:467–510

Vollmers H (2001) Detection of vortices and quantitative evaluation of their main parameters from experimental velocity data. Meas Sci Technol 12:1199–1207

Walther J, Guenot M, Machefaux E, Rasmussen J, Chatelain P, Okulov V, Sørensen J, Bergdof M, Koumoutsakos P (2007) A numerical study of the stability of helical vortices using vortex methods. J Phys Conf Ser 75:012034

Whale J (1996) A study of the near wake of a model wind turbine using particle image velocimetry. PhD, The University of Edinburgh

Whale J, Helmis C, Papadopolous K, Anderson C, Skyner D (1996) A study of the near wake structure of a wind turbine comparing measurements from laboratory and full scale measurements. Sol Energy 56(6):621–633

Whale J, Anderson C, Bareiss R, Wagner S (2000) An experimental and numerical study of the vortex structure in the wake of a wind turbine. J Wind Eng Ind Aerodyn 84:1–21

Widnall S (1972) The stability of a helical vortex filament. J Fluid Mech 54(4):641–663

Yoshida S (2006) Performance of downwind turbines in complex terrain. Wind Eng 30(6):487–502

Zahle F, Sørensen N (2011) Characterisation of the unsteady flow in the nacelle region of a modern wind turbine. Wind Energy 14:271–283

Zhou J, Adrian R, Balachandar S, Kendall T (1999) Mechanisms for generating coherent packets of hairpin vortices in channel flow. J Fluid Mech 387:353–396